Diffuse optical cortical mapping using the boundary element method

Josias Elisee,[1,*] **Adam Gibson,**[1] **and Simon Arridge**[1]

[1]*Center for Medical Image Computing, Department of Computer Science and Department of Medical Physics, University College London, LONDON WC1E 6BT, UK*

**j.elisee@cs.ucl.ac.uk*

Abstract: Cortical mapping, also called optical topography is a new medical imaging modality which allows the non-invasive investigation of the outer layers of the cortex. This technique is challenging and the geometry of the subject is very often over-simplified. We aim here to localize activated regions of an anatomically accurate brain. A Boundary Element Method is used for the forward model. The reconstruction of perturbations in the absorption coefficient is demonstrated in a geometrically realistic simulation and in vivo. These results show that diffuse optical imaging of the head can provide reliable activity maps when anatomical data is available.

OCIS codes: (110.0113) Imaging through turbid media; (110.3200) Inverse scattering; (170.3010) Image reconstruction techniques.

References and links

1. H. Koizumi, T. Yamamoto, A. Maki, Y. Yamashita, H. Sato, H. Kawaguchi, and N. Ichikawa, "Optical Topography: Practical Problems and New Applications," Appl. Opt. **42**, 3054–3062 (2003).
2. R. Weissleder and M. J. Pittet, "Imaging in the era of molecular oncology," Nature **452**, 580–589 (2008).
3. S. R. Arridge, "Optical tomography in medical imaging," Inv. Probl. **15**, R41–R93 (1999).
4. T. Shinba, M. Nagano, N. Kariya, K. Ogawa, T. Shinozaki, S. Shimosato, and Y. Hoshi, "Near-infrared spectroscopy analysis of frontal lobe dysfunction in schizophrenia," Biol. Psychiatry **55**, 154–164 (2004).
5. T. Suto, M. Fukuda, M. Ito, T. Uehara, and M. Mikuni, "Multichannel near-infrared spectroscopy in depression and schizophrenia: cognitive brain activation study," Biol. Psychiatry **55**, 501–511 (2004).
6. A. A. Baird, J. Kagan, T. Gaudette, K. A. Walz, N. Hershlag, and D. A. Boas, "Frontal Lobe Activation during Object Permanence: Data from Near-Infrared Spectroscopy," Neuroimage **16**, 1120 – 1126 (2002).
7. Y. Hoshi and S.-J. Chen, "Regional cerebral blood flow changes associated with emotions in children," Pediatr. Neurol. **27**, 275–281 (2002).
8. R. P. Kennan, D. Kim, A. Maki, H. Koizumi, and R. T. Constable, "Non-Invasive Assessment of Language Lateralization by Transcranial Near Infrared Optical Topography and Functional MRI," Hum. Brain Mapp. **16**, 183–189 (2002).
9. H. Koizumi, A. Maki, and T. Yamamoto, "Optical topography: Practical problems and novel applications," in "Biomedical Topical Meeting," (Optical Society of America, 2002), p. MC1.
10. M. Pena, A. Maki, D. Kovacic, G. Deheane-Lambertz, H. Koizumi, F. Bouquet, and J. Mehler, "Sounds and Silence: An Optical Topography study of Language Recognition at Birth," Proc. Natl. Acad. Sci. U.S.A. **100**, 11702–11705 (2003).
11. K. Liu, D. S. Borrett, A. Cheng, D. Gasparro, and H. C. Kwan, "Near-Infrared Spectroscopy Study of Language Activated Hyper- and Hypo-Oxygenation in Human Prefrontal Cortex," Int. J. Neurosci. **118**, 657–666 (2008).
12. T. Ota, K. Kamada, K. Kawai, M. Yumoto, and N. Saito, "Noninvasive determination of language dominance using multiple functional brain imaging," Neuroimage **47**, S120 (2009), Organization for Human Brain Mapping 2009 Annual Meeting.
13. H. Sato, T. Takeuchi, and K. L. Sakai, "Temporal cortex activation during speech recognition: an optical topography study," Cognition **73**, B55–B66 (1999).

#137913 - $15.00 USD Received 9 Nov 2010; revised 20 Jan 2011; accepted 25 Jan 2011; published 11 Feb 2011

14. D. T. Delpy, M. Cope, P. van der Zee, S. R. Arridge, S. Wray, and J. Wyatt, "Estimation of optical pathlength through tissue from direct time of flight measurement," Phys. Med. Biol. **33**, 1433 (1988).
15. N. L. Everdell, A. P. Gibson, I. D. C. Tullis, T. Vaithianathan, J. C. Hebden, and D. T. Delpy, "A frequency multiplexed near-infrared topography system for imaging functional activation in the brain," Rev. Sci. Instrum. **76**, 093705 (2005).
16. T. J. Germon, P. D. Evans, N. J. Barnett, P. Wall, A. R. Manara, and R. J. Nelson, "Cerebral near infrared spectroscopy: emitter-detector separation must be increased," Br. J. Anaesth. **82**, 831–837 (1999).
17. P. W. McCormick, M. Stewart, M. G. Goetting, M. Dujovny, G. Lewis, and J. I. Ausman, "Noninvasive cerebral optical spectroscopy for monitoring cerebral oxygen delivery and hemodynamics," Crit. Care Med. **19**, 89–97 (1991).
18. D. Contini, A. Torricelli, A. Pifferi, L. Spinelli, F. Paglia, and R. Cubeddu, "Multi-channel time-resolved system for functional near infrared spectroscopy," Opt. Express **14**, 5418–5432 (2006).
19. J. C. Hebden, A. Gibson, R. M. Yusof, N. Everdell, E. M. C. Hillman, D. T. Delpy, S. R. Arridge, T. Austin, J. H. Meek, and J. S. Wyatt, "Three-dimensional optical tomography of the premature infant brain," Phys. Med. Biol. **47**, 4155–4166 (2002).
20. A. P. Gibson, T. Austin, N. L. Everdell, M. Schweiger, S. R. Arridge, J. H. Meek, J. S. Wyatt, D. T. Delpy, and J. C. Hebden, "Three-dimensional whole-head optical tomography of passive motor evoked responses in the neonate," Neuroimage **30**, 521–528 (2006).
21. M. Kacprzak, A. Liebert, P. Sawosz, N. Zolek, and R. Maniewski, "Time-resolved optical imager for assessment of cerebral oxygenation," J. Biomed. Opt. **12**, 034019 (2007).
22. A. Pifferi, A. Torricelli, L. Spinelli, D. Contini, R. Cubeddu, F. Martelli, G. Zaccanti, A. Tosi, A. Dalla Mora, F. Zappa, and S. Cova, "Time-resolved diffuse reflectance using small source-detector separation and fast single-photon gating," Phys. Rev. Lett. **100**, 138101 (2008).
23. H. Wabnitz, M. Moeller, A. Liebert, A. Walter, R. Macdonald, H. Obrig, J. Steinbrink, R. Erdmann, and O. Raitza, "A time-domain nir brain imager applied in functional stimulation experiments," in "Photon Migration and Diffuse-Light Imaging II," (Optical Society of America, 2005), p. WA5.
24. E. Okada, M. Firbank, M. Schweiger, S. R. Arridge, M. Cope, and D. T. Delpy, "Theoretical and experimental investigation of near-infrared light propagation in a model of the adult head," Appl. Opt. **36**, 21–31 (1997).
25. Y. Fukui, Y. Ajichi, and E. Okada, "Monte carlo prediction of near-infrared light propagation in realistic adult and neonatal head models," Appl. Opt. **42**, 2881–2887 (2003).
26. A. Liebert, H. Wabnitz, J. Steinbrink, H. Obrig, M. Möller, R. Macdonald, A. Villringer, and H. Rinneberg, "Time-resolved multidistance near-infrared spectroscopy of the adult head: Intracerebral and extracerebral absorption changes from moments of distribution of times of flight of photons," Appl. Opt. **43**, 3037–3047 (2004).
27. T. S. Leung, C. E. Elwell, and D. T. Delpy, "Estimation of cerebral oxy- and deoxy-haemoglobin concentration changes in a layered adult head model using near-infrared spectroscopy and multivariate statistical analysis," Phys. Med. Biol. **50**, 5783–5798 (2005).
28. T. Nakahachi, M. Iwase, L. Canuet, H. Takahashi, R. Kurimoto, K. Ikezawa, M. Azechi, R. Sekiyama, E. Honaga, C. Uchiumi, M. Iwakiri, N. Motomura, and M. Takeda, "Frontal Activity during the Digit Symbol Substitution Test Determined by Multichannel Near-Infrared Spectroscopy," Neuropsychobiology **57**, 151–158 (2008).
29. F. Abdelnour, B. Schmidt, and T. J. Huppert, "Topographic localization of brain activation in diffuse optical imaging using spherical wavelets," Phys. Med. Biol. **54**, 6383 (2009).
30. F. Abdelnour and T. Huppert, "A random-effects model for group-level analysis of diffuse optical brain imaging," Biomed. Opt. Express **2**, 1–25 (2011).
31. B. Fischl, M. I. Sereno, and A. M. Dale, "Cortical surface-based analysis: Ii: Inflation, flattening, and a surface-based coordinate system," Neuroimage **9**, 195–207 (1999).
32. Y. Tong and B. Frederick, "Using fmri analysis tools (fsl/freesurfer) to analyze near-infrared imaging of the brain," Neuroimage **47**, S58 (2009), Organization for Human Brain Mapping 2009 Annual Meeting.
33. A. Custo, D. A. Boas, D. Tsuzuki, I. Dan, R. Mesquita, B. Fischl, W. E. L. Grimson, and W. W. III, "Anatomical atlas-guided diffuse optical tomography of brain activation," Neuroimage **49**, 561–567 (2010).
34. M. Caffini, A. Torricelli, R. Cubeddu, A. Custo, J. Dubb, and D. A. Boas, "Validating an anatomical brain atlas for analyzing nirs measurements of brain activation," in "Digital Holography and Three-Dimensional Imaging," (Optical Society of America, 2010), p. JMA87.
35. D. Yao, "High-resolution EEG Mapping : an Equivalent Charge-Layer Approach," Phys. Med. Biol. **48**, 1997–2011 (2003).
36. B. He, x. Zhang, J. Lian, H. Sasaki, D. Wu, and V. L. Towle, "Boundary Element Method-Based Cortical Potential Imaging of Somatosensory Evoked Potentials Using Subjects' Magnetic Resonance Images," Neuroimage **16**, 564–576 (2002).
37. J. Ollikainen, M. Vauhkonen, P. Karjalainen, and J. Kaipio, "A new computational approach for cortical imaging," IEEE Trans. Med. Im. **20**, 325–332 (2001).
38. J. Elisee, A. Gibson, and S. Arridge, "Combination of boundary element method and finite element method in diffuse optical tomography," IEEE Trans. Biomed. Eng. **57**, 2737–2745 (2010).
39. J. Sikora, A. Zacharopoulos, A. Douiri, M. Schweiger, L. Horesh, S. Arridge, and J. Ripoll, "Diffuse photon

#137913 - $15.00 USD Received 9 Nov 2010; revised 20 Jan 2011; accepted 25 Jan 2011; published 11 Feb 2011

propagation in multilayered geometries," Phys. Med. Biol. **51**, 497–516 (2006).
40. M. Schweiger, S. R. Arridge, and I. Nissila, "Gauss-newton method for image reconstruction in diffuse optical tomography," Phys. Med. Biol. **50**, 2365 (2005).
41. S. R. Arridge and M. Schweiger, "Photon measurement density functions. Part 2: Finite element calculations," Appl. Opt. **34**, 8026–8037 (1995).
42. A. Tizzard, L. Horesh, R. J. Yerworth, D. S. Holder, and R. H. Bayford, "Generating Accurate Finite Element Meshes for the Forward Model of he Human Head in EIT," Physiol. Meas. **26**, S251 (2005).
43. J. C. Hebden and T. Austin, "Optical tomography of the neonatal brain," Eur. Radiol. **17**, 2926–2933 (2007).
44. A. P. Gibson, J. Riley, M. Schweiger, J. C. Hebden, S. R. Arridge, and D. T. Delpy, "A method for generating patient-specific finite element meshes for head modelling," Phys. Med. Biol. **48**, 481–495 (2003).
45. E. Widmaier, H. Raff, and K. Strang, *Vander's human physiology: the mechanisms of body function*, p. 306 (McGraw-Hill Higher Education, 2008).
46. J. Selb, J. J. Stott, M. A. Franceschini, A. G. Sorensen, and D. A. Boas, "Improved sensitivity to cerebral hemodynamics during brain activation with a time-gated optical system: analytical model and experimental validation," J. Biomed. Opt. **10**, 011013 (2005).
47. M. Butti, D. Contini, E. Molteni, M. Caffini, L. Spinelli, G. Baselli, A. M. Bianchi, S. Cerutti, R. Cubeddu, and A. Torricelli, "Effect of prolonged stimulation on cerebral hemodynamic: A time-resolved fnirs study," Med. Phys. **36**, 4103–4114 (2009).
48. H. Wabnitz, M. Moeller, A. Liebert, H. Obrig, J. Steinbrink, and R. Macdonald, *Oxygen Transport to Tissue XXXI* (Springer US, 2010), vol. 662 of *Biomedical and Life Sciences*, chap. Time-Resolved Near-Infrared Spectroscopy and Imaging of the Adult Human Brain, pp. 143–148.

1. Introduction

The monitoring of brain activity through novel, less costly, more tuneable and more versatile techniques is a major trend in neuroimaging. We concentrate here on cortical mapping, also called optical topography [1]. Unlike the more widely investigated diffuse optical tomography (DOT [2, 3]) which allows to recover three dimensional distributions of the optical parameters, cortical mapping concentrates on the surface region of the brain closest to the skull. Cortical mapping is a relatively new technique and is mainly applied to relate superficial brain activity to high cognitive processes such as in the study of mental illnesses [4, 5], developmental psychology [6–10] and linguistics [11–13].

In all optical topography/cortical mapping/near-infrared spectroscopy (NIRS) problems, the quantity which is monitored is the Hemoglobin/Total Hemoglobin ratio (HbO_2/Hb_{total}) or the Deoxy-Hemoglobin/Total Hemoglobin ratio closely related to the absorption coefficient. It gives an insight on the oxygenation and can indirectly measure the activation of a region. In order to find this coefficient, the medium is illuminated with a known source and detectors are placed on the surface to record the response of the domain within the continuous wave (attenuation), frequency domain (amplitude and phase) or time domain (Temporal Point Spread Function, TPSF [14]) frameworks.

Most of the theory which allows one to infer the absorption coefficient from photon density measurements is based on the modified Beer-Lambert law [14]. Such considerations allow the use of DC-intensity, continuous wave instruments to find the oxygenation ratio in tissue. They are currently the most readily available commercially and versions with large number of source-detector couples exist [15–17].

Use of a time-resolved instrument, on the other hand, offsets a smaller number of source-detector pairs against the increased information content of the time-resolved data [18–23].

The human brain, when probed with a NIR device, behaves like a multi-layered geometry, which is often considered as a slab [24]. This biological tissue is very thick for near-infrared light to pass through. Experimentally, this value varies between 5 and 10 mm [25] or slightly more [26] up to 15-20 mm. This is very close to the size of the extracerebral layers, which varies between 8 [26] and 14 mm [27]. It means that only the superficial layer of the adult brain (cortex) is imaged.

Currently, most of the studies involving near-infrared investigation of the brain do not include

#137913 - $15.00 USD Received 9 Nov 2010; revised 20 Jan 2011; accepted 25 Jan 2011; published 11 Feb 2011

an anatomical model in the reconstruction computation. Instead a reconstruction in a simplified geometry is followed by registration to an MRI based geometry as a post-processing step, and can lead to inaccurate localisation and/or quantisation.

We aim here to use the anatomical information as a constraint of the inverse problem. This objective manifests itself in the restriction of the reconstructed region to the surface of the brain and our multi-layered model.

Current successful optical topography systems are similar to devices like the Hitachi ETG-4000 which is able to image up to 52 channels at the same time [28]. They have been widely used and shown to produce results of interest in clinical and psychological research. However, despite the success of this technology, it is possible to improve many aspects of the output (localisation, spatial resolution, quantitation, repetability) by including anatomical data in the reconstruction process.

As far as accuracy is concerned, the best studies so far have relied on MRI-derived data and analysis methods. F. Abdelnour *et al.* [29, 30], for example, have used a Finite Element Method (FEM) model for the propagation of light through tissue in a biologically accurate 5 tissue types model of the head. The fidelity to the anatomical features was ensured by the use of a well-known MRI tool, Freesurfer [31] which contains an atlas of the adult head. However, since the FEM gives a volume solution, the surface one has to be extracted in order to perform actual cortical mapping. Our model aims to simplify a similar process by integrating the photon density on the volume within the model itself. The solution that it outputs is a surface density. Another example of a multi-modality combination is found in a study by Y. Tong and B. Frederick [32] where the fMRI (functional MRI) analysis tools have been used with the Blood-Oxygen-Level Dependent (BOLD) signal being replaced by the fNIRS (functional NIRS) data. Studies by Custo *et al.* [33] and Caffini *et al.* [34] also show the successful use of MRI-derived data for the geometry of the adult head in a similar context.

In this paper, we reconstruct an in vivo experiment uses an atlas mesh built from MRI data. Using a boundary element method (BEM), we develop a model for the mapping of photon densities between surfaces of the multilayer representation, thus reconstructing what we introduce as an *Equivalent Cortical Absorption* $\left(\mu_{\mathrm{a}}^{\mathrm{ECA}}\right)$. Our method suggests that it is possible to overcome the fundamental limitations of functional optical topography and obtain reliable maps of the cortex with a simple and fast algorithm.

2. Diffuse optical cortical mapping

In principle, functional optical tomography can be achieved using a volume based approach and full tomographic data obtained over a large part of the head [19, 20]. In the limit of 'complete' data measured for all possible source and detector combinations over a closed surface, the inverse problem technically has a unique solution. However, the strong ill-posedness of the problem coupled with the limited amount of available data means that the reconstructed solutions are prone to artefacts and require substantial regularisation. In Diffuse Optical Cortical Mapping (DOCM) we propose instead the replacement of a volume image of activation with a surface map on the cortex. This idea is analogous with the inverse problem of Electroencephalography in which volume charges and currents in the brain are represented by an equivalent charge or dipole layer [35]. In that problem, only direct imaging of the potential arising from current sources induced by functional activation are measured and the problem is both ill-posed and non-unique; sources reconstructed onto an equivalent source layer are then forward mapped onto the cortical source for effective imaging of the equivalent cortical surface source distribution. An alternative to this strategy is to directly derive a cortical potential image by considering the mapping

$$U^{\mathrm{scalp}} = \mathscr{T} U^{\mathrm{cortex}} \tag{1}$$

#137913 - $15.00 USD Received 9 Nov 2010; revised 20 Jan 2011; accepted 25 Jan 2011; published 11 Feb 2011

where $\mathscr{T}$ is known as the cortex-scalp transfer map [36,37]. It has the form of a (nonstationary) blurring operation. In the case of discrete measurments the mapping becomes

$$y^{\text{scalp}} = \mathscr{M}\mathscr{T}U^{\text{cortex}} \tag{2}$$

where $\mathscr{M}$ represents the sampling of the potential U^{scalp} at a set of detectors. The inversion of the linear operator $\mathscr{M}\mathscr{T}$ is underdetermined and ill-posed and requires regularisation. To derive the equivalent theory for DOCM, we first recall some principles of the Boundary Element Method for this application

2.1. BEM forward model theory

For a system of $n+1$ nested layers, $\Omega_0 \ldots \Omega_n$, with interfaces $\Gamma_0 \ldots \Gamma_n$ the BEM system is written [38,39],

$$\begin{pmatrix} \mathsf{K}_{00} & \mathsf{K}_{01} & \cdots & \cdots \\ \mathsf{K}_{10} & \mathsf{K}_{11} & \mathsf{K}_{12} & \cdots \\ \vdots & \vdots & \vdots & \ddots \\ \cdots & \cdots & \mathsf{K}_{\ell\ell'} & \cdots \\ \vdots & \vdots & \vdots & \ddots \\ \cdots & \cdots & \mathsf{K}_{nn-1} & \mathsf{K}_{nn} \end{pmatrix} \begin{pmatrix} \Phi^{(0)} \\ \Phi^{(1)} \\ J^{(1)} \\ \vdots \\ \Phi^{(\ell')} \\ J^{(\ell')} \\ \vdots \\ \Phi^{(n)} \\ J^{(n)} \end{pmatrix} = Q \tag{3}$$

with $\Phi^{(\ell)}, J^{(\ell)}$ representing the vectors of photon density and photon current on interface Γ_ℓ, and Q representing the source term. The matrix blocks $\mathsf{K}_{\ell\ell'}$ represent the discretisation of the single and double layer potential operators $\mathscr{A}^{\text{SL}}, \mathscr{A}^{\text{DL}}$ that couple a function and its normal derivative on the boundary of a domain with the Green's function in the interior of that domain. In particular, for the diffusion equation model used in this paper, for optical parameters defined in terms of absorption coefficient μ_{a} and reduced scattering coefficient μ_{s}' we define the Green's function in the ℓ^{th} layer, as

$$G_\ell(\mathbf{r},\mathbf{r}') = \frac{1}{4\pi}\frac{e^{-\varpi_\ell|\mathbf{r}-\mathbf{r}'|}}{|\mathbf{r}-\mathbf{r}'|} \tag{4}$$

with $\varpi_\ell = \left(\frac{\mu_{\text{a},\ell}+\frac{\mathrm{i}\omega}{c}}{D_\ell}\right)^{1/2}$ being the wave number and $D_\ell = \frac{1}{3(\mu_{\text{a},\ell}+\mu'_{\text{s},\ell})}$ the diffusion coefficient. For a surface Γ_ℓ with a mesh consisting of nodes $\{N_{\ell,k}, k = 1 \ldots n_{\Gamma_\ell}\}$ and basis functions $\{\phi_{\ell,k}, k = 1 \ldots n_{\Gamma_\ell}\}$ the component matrices $\mathsf{A}^{\text{SL}}_{ll'}, \mathsf{A}^{\text{DL}}_{ll'}$ are given by surface integrals

$$A^{\text{SL}}_{ll'}(k,k') = \int_{\Gamma_{\ell'}} \frac{G_\ell(N_{\ell',k},\mathbf{r}')}{D_\ell}\phi_{\ell',k}(\mathbf{r}')\mathrm{d}S(\mathbf{r}') \tag{5}$$

$$A^{\text{DL}}_{ll'}(k,k') = \int_{\Gamma_{\ell'}} \frac{\partial G_\ell(N_{\ell',k},\mathbf{r}')}{\partial \nu_\ell}\phi_{\ell',k}(\mathbf{r}')\mathrm{d}S(\mathbf{r}') \tag{6}$$

from which $\mathsf{K}_{\ell\ell'}$ are constructed by linear combination [38,39].

For the calculation of the probe fields we consider S inward directed photon currents at source

#137913 - $15.00 USD Received 9 Nov 2010; revised 20 Jan 2011; accepted 25 Jan 2011; published 11 Feb 2011

locations $\{\mathbf{r}_j, j = 1 \ldots S\}$ so that

$$Q_j = \begin{pmatrix} Q_j^{(0)} \\ 0 \\ 0 \\ \vdots \\ 0 \end{pmatrix} . \tag{7}$$

Solution of the BEM system Eq. (3) for each input source generates the cortical photon probe densities $\{\Phi_j^{\text{cortex}}, j = 1 \ldots S\}$.

Now consider the secondary sources given by the product of the probe fields and the activation in the brain, which, using Green's identity, become

$$Q_j^{\text{actvn}} = \begin{pmatrix} 0 \\ 0 \\ 0 \\ \vdots \\ Q_j^{(n)} \end{pmatrix} , \qquad \text{where} \quad Q_j^{(n)}(\mathbf{r}) = \int_{\Omega_n} G_n(\mathbf{r}, \mathbf{r}') \mu_{\text{a}}^{\text{actvn}}(\mathbf{r}') \Phi_j^{(n)}(\mathbf{r}') \mathrm{d}\mathbf{r}' \tag{8}$$

where $\Phi_j^{(n)}(\mathbf{r}')$ is the solution density in the n^{th} layer for the source j. When dealing with nested BEM regions representing a head, Ω_n is the brain or the innermost region. Solution of Eq. (3) with the secondary sources Q_j^{actvn} results in the secondary density Φ_j^{actvn}. The equivalent cortical absorption is therefore modeled by

$$\Phi_j^{\text{actvn}} = \mu_{\text{a}}^{\text{ECA}} \Phi_j^{\text{cortex}} . \tag{9}$$

Applying the transfer matrix and the measurement operator gives the measured activation signal

$$y_j^{\text{actvn}} = \mathscr{M}_j \mathscr{T} \mu_{\text{a}}^{\text{ECA}} \Phi_j^{\text{cortex}} . \tag{10}$$

The transfer operator $\mathscr{T}$ does not depend on the sources or measurements. It can be calculated from the BEM matrix by repeated application of the Schur complement to eliminate all the unknowns in Eq. (3) except for the cortical and scalp photon densities. We give an explicit form of the matrix representation T for an n+1 layer layer system in the Appendix.

Combining data from all of the S sources gives rise to a stacked operator

$$\begin{pmatrix} y_1^{\text{actvn}} \\ y_2^{\text{actvn}} \\ \vdots \\ y_S^{\text{actvn}} \end{pmatrix} = \begin{pmatrix} \mathscr{M}_1 \mathsf{T} \mathrm{diag}\left[\Phi_1^{\text{cortex}}\right] \\ \mathscr{M}_2 \mathsf{T} \mathrm{diag}\left[\Phi_2^{\text{cortex}}\right] \\ \vdots \\ \mathscr{M}_S \mathsf{T} \mathrm{diag}\left[\Phi_S^{\text{cortex}}\right] \end{pmatrix} \mu_{\text{a}}^{\text{ECA}} \qquad \equiv \quad y^{\text{actvn}} = \mathsf{W} \mu_{\text{a}}^{\text{ECA}} \tag{11}$$

The computational cost of constructing the linear Jacobian matrix W in Eq. (11) is the cost of the S solutions of Eq. (3) for the probe fields. We may alternatively construct W by an adjoint method by solving Eq. (3) for M adjoint sources located at the detector positions, to give adjoint fields $\Phi_i^{\text{cortex},*}, i = 1 \ldots M$ as described in [38] and constructing the row of W corresponding to source j and detector i as

$$w_{ij} = \Phi_i^{\text{cortex},*} \Phi_j^{\text{cortex}} \tag{12}$$

The adjoint method was employed in this paper.

Further, we consider the scenario in [20], wherein the measurements are the logarithmic amplitude $\ln A$ and phase θ of the complex valued density Φ^{scalp}. The experimental derivation of

#137913 - $15.00 USD Received 9 Nov 2010; revised 20 Jan 2011; accepted 25 Jan 2011; published 11 Feb 2011

the data is obtained using a time-domain measurement system, followed by Fourier transformation and sampling at a single modulation frequency [20]. This gives rise to a splitting of the data (y) and Jacobian ;

$$\begin{pmatrix} y^{\ln A} \\ y^{\theta} \end{pmatrix} = \begin{pmatrix} \mathrm{Re} \\ \mathrm{Im} \end{pmatrix} \log y = \begin{pmatrix} \mathrm{Re} \\ \mathrm{Im} \end{pmatrix} \mathrm{diag}\left[\frac{1}{y}\right] \mathsf{W}\mu_{\mathrm{a}}^{\mathrm{ECA}} \tag{13}$$

2.2. Inverse problem

Since the matrix W is ill conditioned we consider a regularised solution as the minimiser of the weighted norm

$$||y - \mathsf{W}\mu_{\mathrm{a}}^{\mathrm{ECA}}||^2_{\mathsf{C}_y^{-1}} + \alpha R(\mu_{\mathrm{a}}^{\mathrm{ECA}}) \rightarrow \min \tag{14}$$

where C_y^{-1} is the inverse covariance matrix of the assumed measurement noise model and $R(\mu_{\mathrm{a}}^{\mathrm{ECA}})$ is a regularising functional. In this paper we take the simple zero-order Tikhonov regulariser which leads to the linear inversion:

$$(\mathsf{W}^{\mathrm{T}}\mathsf{C}_y^{-1}W + \alpha \mathsf{I})\ \mu_{\mathrm{a}}^{\mathrm{ECA}} = \mathsf{W}^{\mathrm{T}}\mathsf{C}_y^{-1}y^{\mathrm{actvn}}. \tag{15}$$

As in [38] we here take $\mathsf{C}_y^{-1} = \mathrm{diag}\left[1/\overline{\ln \mathrm{A}}, 1/\overline{\theta}\right]$, where $\overline{\ln \mathrm{A}}$ and $\overline{\theta}$ are the average initial errors in log ampliture and phase respectively [40].

Equation (15) is solved using the MINRES solver in MATLAB with a tolerance of 10^{-6}.

3. Results

3.1. Simulation

We begin the investigation of the accuracy of our method by testing on a simulation case. The same meshes, optical properties and optode placement were used for the simulation as in the in-vivo case in section 3.2. We use a 3-layer BEM mesh composed of 2806 surface nodes and 1402 surface elements for the scalp layer, 3294 surface nodes and 1646 surface elements for the skull layer, 2098 surface nodes and 1048 surface elements for the brain region. Accuracy of the BEM forward model has been tested in [38, 39]. The optical parameters were close to a neonatal human head $\mu_{\mathrm{s}}^{\prime\,\mathrm{brain}} = 0.61mm^{-1}$, $\mu_{\mathrm{a}}^{\mathrm{brain}} = 0.014mm^{-1}$, $\mu_{\mathrm{s}}^{\prime\,\mathrm{skull}} = 0.625mm^{-1}$, $\mu_{\mathrm{a}}^{\mathrm{skull}} = 0.024mm^{-1}$ and $\mu_{\mathrm{s}}^{\prime\,\mathrm{scalp}} = 1.4mm^{-1}$, $\mu_{\mathrm{a}}^{\mathrm{scalp}} = 0.016mm^{-1}$. The optodes set consisted of 12 sources and 30 detectors, as presented earlier in [38]. 258 measurements were kept for the analysis out of the 360 possible ones. A spherical inclusion with $\mu_{\mathrm{a}}^{\mathrm{inclusion}} = 0.034mm^{-1}$ and of diameter 10mm was put inside the brain layer and moved along a surface normal deeper inside the mesh. The BEM-FEM model of [38] was used to generate the data and 1% of white noise was added to it. The regularisation parameter was set to $\alpha = 1.72 \times \mathrm{Tr}[\mathsf{W}^{\mathrm{T}}\mathsf{W}]$.

The Figs. 1 and 2 show a trend of contrast increasing and diminishing, as the blob varies in overlap with the Photon Measurement Density Function [41] of the optodes. As it moves deeper inside the brain, the contrast decreases and the noise is reconstructed instead.

The pictures in Figs. 1 and 3 have been generated by a projection of the solution on a higher resolution brain mesh of 13498 surface nodes mesh for improved visualisation. Both the coarse and fine resolution meshes were obtained from a model using data from MRI scans of a neonate, courtesy of A. Tizzard *et al.* [42].

The projection between meshes was implemented using the following steps:

1. Rigid body registration of the low and high resolution brain meshes;
2. Reparametrisation of both brain meshes to spherical coordinates;

#137913 - $15.00 USD Received 9 Nov 2010; revised 20 Jan 2011; accepted 25 Jan 2011; published 11 Feb 2011

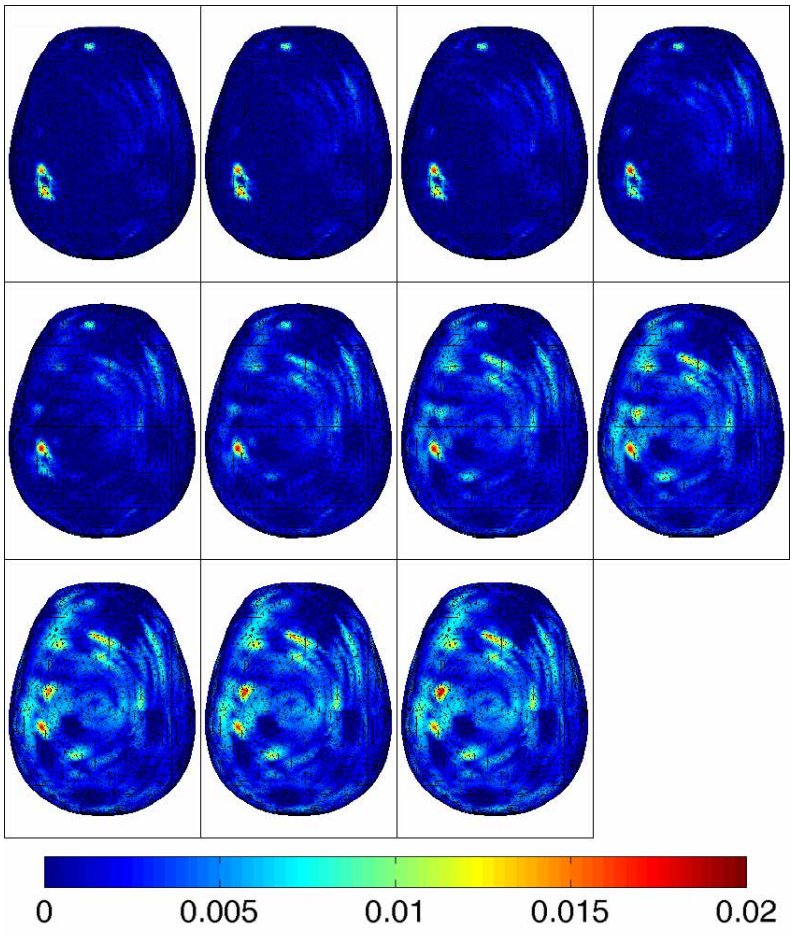

Fig. 1. Left to right and top to bottom, reconstructions of a Gaussian absorption target simulated with the FEM (1% noise). The target is moved by 2mm from the surface of the brain (top left) to 20mm below the surface.

3. Linear interpolation on the sphere of the values on the coarse mesh's nodes onto the fine mesh's nodes using an equal-area planar map projection;

4. Reprojection of the fine mesh's sphere to the fine brain mesh by converting back to Cartesian coordinates.

3.2. In vivo reconstruction

After the successful testing of the method on simulation we went on to apply it on data from an *in vivo* motor response study on pre-term babies as reported in [20, 43].

As the 33 weeks old neonate is sleeping, his arm is moved: this stimulus activates an area of the brain corresponding to the action, here the motor and somatosensory cortices. Such a technique allows to use the linear reconstruction theory, since we can have the data before (reference rest state) and during the movement. In the present case, it is the right arm which is moved.

#137913 - $15.00 USD Received 9 Nov 2010; revised 20 Jan 2011; accepted 25 Jan 2011; published 11 Feb 2011

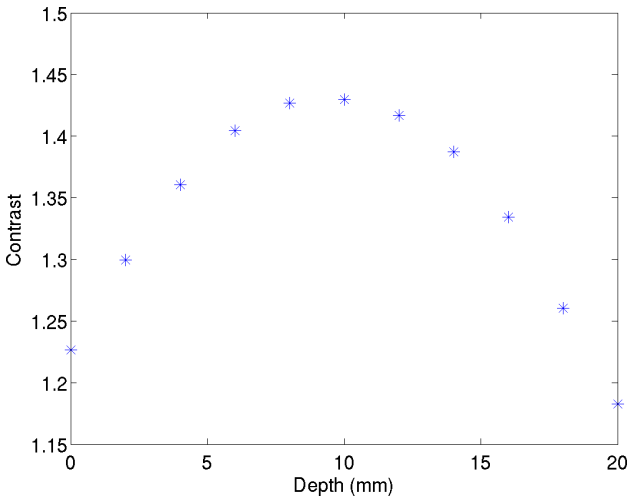

Fig. 2. Evolution of the contrast, i.e. the difference absorption of the target divided by the background absorption. The nominal value is 1.43.

In such an experiment, due to the setup and the nature of the subject, one only has the position of the sources and detectors relative to an absolute origin. The actual attitude of the baby has to be inferred from this data. The mesh is then warped onto the measurement cap using a method in three steps:

1. Rigid body translation, rotation and stretching of the surface in 3D so that it comes relatively close to the optodes and passes through the space spanned by the optodes
2. Identification of the closest nodes to each optode on the surface mesh
3. Application of a nonlinear thin-plate spline deformation which causes the surface mesh to pass through all the optodes

The details of this method can be found in an article by A. Gibson *et al.* [44].

In a previous publication [20], the motor cortex's activation was reconstructed with a resolution of 10mm. As it can be seen in Fig. 3, the activation has been localized on the brain surface. The regularisation parameter was set to $\alpha = 0.97 \times \mathrm{Tr}[\mathrm{W}^{\mathrm{T}}\mathrm{W}]$. The lateralization of the movement manifests itself by an increase in absorption in the hemisphere involved. A spatial full-width at half maximum (FWHM) of 6mm is observed for the equivalent cortical absorption due to activation. It shows that our method is able to provide qualitatively reliable cortical mapping results, localized and characterized.

The relation between the quantitative reconstruction and the volume absorption activation is determined by the volume convolution in Eq. (8), and varies with depth.

4. Discussion and conclusions

We developed a cortical mapping method able to localize the perturbations to the NIR signal originated from activation in the brain. By testing it on simulated and *in vivo* data, we demonstrated its ability to accurately find the position of the part of these perturbations which is on the surface of the cortex.

With our simple surfaces-based model, we did not explicitly model the influence of the CSF, although this is also possible within a BEM framework. Instead we restricted the reconstruction

#137913 - $15.00 USD Received 9 Nov 2010; revised 20 Jan 2011; accepted 25 Jan 2011; published 11 Feb 2011

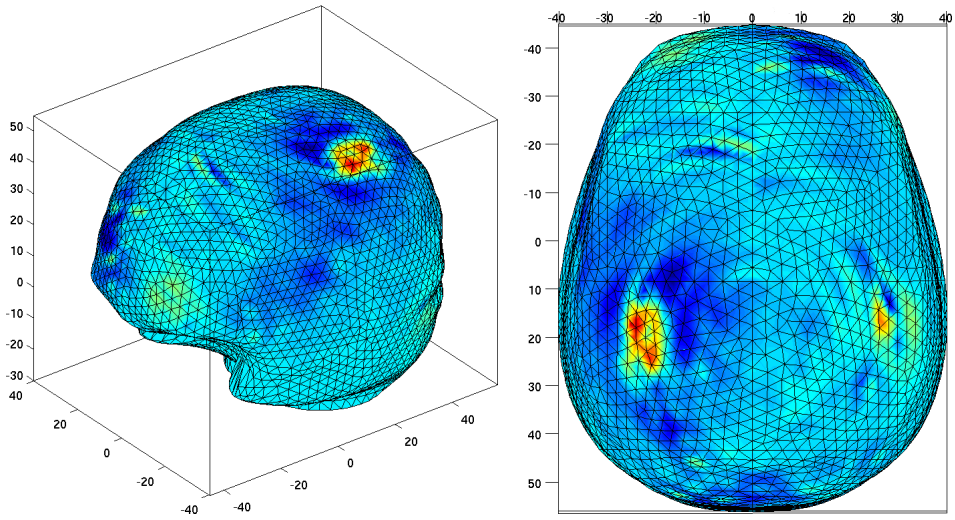

Fig. 3. Side and top views of a cortical map of the activated brain - the primary motor and somatosensory cortices activation is clearly visible. This position corresponds to the arm region as it can be seen in [45].

to the cortex, as this is the key feature of a measurement passing through this region of the brain [24]. With the use of time-gated measurements [46, 47] or the use of the variance of the TPSF [48], the signal could be reliably restricted to the brain surface. This will be the subject of an upcoming publication.

Setting up the BEM cortical mapping computation is simple, once anatomical data can be obtained. This can be done with the deformation of an existing atlas respective to measured fiducials during the experiment, like in our case, or with the help of individual anatomically-resolved scans (MRI, X-Ray). As soon as a surface mesh is obtained, which is usually the first step taken after segmentation, the BEM cortical mapping can be used. After the initial building of a Jacobian for the problem, subsequent measurements on the same subject could be analysed in real time, since the actual reconstruction time is less than one second.

Appendix : Derivation of transfer matrix in n-layer case

To obtain the mapping in an n+1 layer case, we rewrite the system Eq. (3) as

$$\begin{pmatrix} \mathsf{K}_{00} & [\mathsf{B}] & 0 & 0 \\ [\mathsf{C}] & [\mathsf{D}] & [\mathsf{E}] & [\mathsf{F}] \\ 0 & [\mathsf{G}] & \mathsf{K}_{n-1,n-1} & \mathsf{K}_{n-1,n} \\ 0 & 0 & \mathsf{K}_{n,n-1} & \mathsf{K}_{n,n} \end{pmatrix} \begin{pmatrix} \mathbf{\Phi}^{(0)} \\ [x] \\ \mathbf{\Phi}^{(n)} \\ J^{(n)} \end{pmatrix} = \begin{pmatrix} 0 \\ 0 \\ 0 \\ Q \end{pmatrix} \tag{16}$$

where $[\mathsf{B}], [\mathsf{C}], [\mathsf{D}], [\mathsf{E}], [\mathsf{F}], [\mathsf{G}]$ represent here submatrices of the complete BEM matrix corresponding to the uninteresting parameters.

By elimination of $J^{(n)}$ and Q we can write

$$\left([\mathsf{D}] - [\mathsf{F}]\mathsf{K}_{n-1,n}^{-1}[\mathsf{G}]\right)[x] = \left([\mathsf{E}] - [\mathsf{F}]\mathsf{K}_{n-1,n}^{-1}\mathsf{K}_{n-1,n-1}\right)\mathbf{\Phi}^{(n)} + [\mathsf{C}]\,\mathbf{\Phi}^{(0)} \tag{17}$$

#137913 - $15.00 USD Received 9 Nov 2010; revised 20 Jan 2011; accepted 25 Jan 2011; published 11 Feb 2011

This allows to eliminate $[x]$ from the first row of Eq. (16) and we obtain

$$\left(\mathsf{K}_{00} - [\mathsf{B}]\left([\mathsf{D}] - [\mathsf{F}]\mathsf{K}_{n-1,n}^{-1}[\mathsf{G}]\right)^{-1}[\mathsf{C}]\right)\boldsymbol{\Phi}^{(0)} = [\mathsf{B}]\left([\mathsf{D}] - [\mathsf{F}]\mathsf{K}_{n-1,n}^{-1}[\mathsf{G}]\right)^{-1}\left([\mathsf{E}] - [\mathsf{F}]\mathsf{K}_{n-1,n}^{-1}\mathsf{K}_{n-1,n-1}\right)\boldsymbol{\Phi}^{(n)} \tag{18}$$

The matrix on the left is rank-complete and invertible, leading to the final expression for the transfer matrix

$$\mathsf{T} = \left(\mathsf{K}_{00} - [\mathsf{B}]\mathsf{H}^{-1}[\mathsf{C}]\right)^{-1}[\mathsf{B}]\mathsf{H}^{-1}\left([\mathsf{E}] - [\mathsf{F}]\mathsf{K}_{n-1,n}^{-1}\mathsf{K}_{n-1,n-1}\right) \tag{19}$$

with

$$\mathsf{H} = \left([\mathsf{D}] - [\mathsf{F}]\mathsf{K}_{n-1,n}^{-1}[\mathsf{G}]\right) \tag{20}$$

In a similar way, mappings between other pairs of unknowns can be obtained, and between the cortical densities and the source distribution.

Acknowledgments

The authors would like to acknowledge the contribution of Dr. M. Schweiger and Dr. A. Zacharopoulos for their help in developing the BEM software. This research was supported by EC Seventh Framework programme, grant number: 201792, and by EPSRC grant EP/E034950/1.